Application of high-resolution landmark-free morphometrics to a mouse model of Down Syndrome reveals a tightly localised cranial phenotype

Nicolas Toussaint[1]*, Yushi Redhead[2,3]*, Wei Liu[4], Elizabeth M. C. Fisher[5], Benedikt Hallgrimsson[4], Victor L.J. Tybulewicz[3,6§], Julia A. Schnabel[1§], Jeremy B.A. Green[2§]

[1] School of Biomedical Engineering and Imaging Sciences, King's College London, United Kingdom
[2] Centre for Craniofacial Biology & Regeneration, King's College London, United Kingdom.
[3] The Francis Crick Institute, London NW1 1AT, United Kingdom.
[4] Department of Cell Biology & Anatomy, University of Calgary, Calgary AB T2N 4N1, Canada
[5] Institute of Neurology, University College London, London, WC1N 3BG, United Kingdom.
[6] Department of Immunology & Inflammation, Imperial College London, London W12 0NN, United Kingdom.

*Equal contribution

[§]Correspondence to:
JAS (email: julia.schnabel@kcl.ac.uk), VLJT (email: Victor.T@crick.ac.uk), or to
JBAG (email: jeremy.green@kcl.ac.uk)

Abstract

Characterising phenotypes often requires quantification of anatomical shapes. Quantitative shape comparison (morphometrics) traditionally uses anatomical landmarks and is therefore limited by the number of landmarks and operator accuracy when landmarks are located manually. Here we apply a landmark-free method to characterise the craniofacial skeletal phenotype of the Dp1Tyb mouse model of Down syndrome (DS), validating it against a landmark-based approach. We identify cranial dysmorphologies in Dp1Tyb mice, especially smaller size and brachycephaly (front-back shortening) homologous to the human phenotype. The landmark-free phenotyping was less labour-intensive and required less user training than the landmark-based method. It also enabled mapping of local differences as planar expansion or shrinkage. This higher resolution and local mapping pinpointed reductions in interior mid-snout structures and occipital bones in this DS model that were not as apparent using a traditional landmark-based method. This approach could make morphometrics widely-accessible beyond traditional niches in zoology and palaeontology, especially in characterising mutant phenotypes.

Introduction

Morphometrics, the quantitative comparison of biological shapes, is well established in the fields of palaeontology and evolutionary biology to quantify and understand morphological phenotypes (Cooke and Terhune, 2015). Landmark positions are recorded on digital two- or three-dimensional images (obtained by photography, X-ray or MRI methods) and their spatial distributions are then analysed through Euclidean distance matrix analysis (EDMA) or Procrustes Superimposition (PS) (Webster and Sheets, 2010). Morphometrics is less used in other fields, such as genetics and developmental biology. This may be because current morphometric methodologies, while powerful, have limitations. First, the number of landmarks always reflects a compromise between precision, which needs many anatomical landmarks to be located, and ease-of-use, which limits those numbers. Typically, some tens of landmarks are located manually, which takes anatomical knowledge and training and time. Second, an anatomical landmark may be absent from an individual due to natural variation, engineered mutation or pathology. Third, landmarks can be sparse in anatomical structures where they are hard to define: smooth surfaces do not have easily defined landmarks. Sparseness is a particular problem in soft tissues and embryos, with numerous featureless, curved surfaces. Semi-landmarks interpolated between landmarks (Andresen et al., 2000; Bookstein, 1997; Frangi et al., 2003) reduce this problem but still leave gaps (Palci and Lee, 2019). Fourth, manual landmark-based methods are inevitably susceptible to both inter- and intra-operator variability, which can be as big as the biological variability between subjects (Percival et al., 2014; Shearer et al., 2017; von Cramon-Taubadel et al., 2007). Together, these limitations suggest that there is a need for automated, ideally landmark-free, high-resolution methods. Landmark-free methods have been developed by the neuroimaging community to quantify the size and shape of the brain precisely because its relatively smooth shape hampers the definition of reliable landmarks (Bron et al., 2015; Routier et al., 2014) but these methods have yet to be applied more widely and have not been directly compared to the landmark-based approach.

One of the most common human dysmorphologies is the craniofacial phenotype associated with Down syndrome (DS). Individuals with DS, currently ~1 in 800 births (Antonarakis, 2017), have characteristic features – flattened midface with low nose bridge, front-to-back shortened skull (brachycephaly) and slightly hooded eyelids (Korenberg et al., 1994). Although the craniofacial features affect everyone with DS, this phenotype is not well understood either genetically or developmentally. DS is caused by trisomy of human chromosome 21 (Hsa21) which carries 232 protein-coding genes (Ensembl genome assembly GRCh38) (Antonarakis, 2017; Lejeune et al., 1959). It is thought that the presence of a third copy of one or more of these genes (rather than just the higher chromosomal load) gives rise to the individual defects observed in DS, but the critical dosage-sensitive genes are not known (Lana-Elola et al., 2016; Lana-Elola et al., 2011; Watson-Scales et al., 2018).

To model DS, mouse strains have been engineered that carry an extra copy of each of the three regions of the mouse genome orthologous to Hsa21. These recapitulate at least some aspects of DS (Herault et al., 2017; Lana-Elola et al., 2016; Yu et al., 2010). Morphometrics applied to Ts65Dn (Hill et al., 2007; Richtsmeier et al., 2000; Richtsmeier et al., 2002) and Dp(16)1Yey mice (Starbuck et al., 2014) showed that trisomy of part or all of the Hsa21-orthologous region of mouse chromosome 16 (Mmu16) resulted in craniofacial dysmorphology which resembled the DS phenotype. The cranial dysmorphology in Dp1Yey mice was highly statistically significant (with multiple linear distances between landmarks differing statistically significantly from wild type in all regions measured) yet quantitatively subtle, with an average landmark-to-landmark distance difference of only 7% between mutant and wild-type (WT) control mice (Starbuck et al., 2014).

In this paper, we describe a convenient pipeline we have developed for landmark-free morphometric analysis based on an approach used for brain imaging (Durrleman et al., 2014). We compare our method to the traditional landmark-based morphometric approach, focusing

on the characterisation of the craniofacial phenotype of the Dp1Tyb mouse model of DS which has an additional copy of the entire Hsa21-orthologous region of Mmu16 (Lana-Elola et al., 2016). We find that the landmark-free analysis gives separation by shape between Dp1Tyb and WT mice that is at least as clear as that achieved by landmark-based analysis, while delivering a number of operational advantages. We demonstrate a new tool ("local stretch" mapping) that avoids the need to separate scale changes from shape changes, and localises abnormalities in the DS model to cranial vault expansion and mid-face and occipital contraction.

Results

Landmark-based and landmark-free analysis of Dp1Tyb skulls

To phenotype the Dp1Tyb DS model skulls, we used micro-computed tomography (μCT) to acquire images of the skulls of 16-week old WT and Dp1Tyb mice. We carried out landmark-based analysis in the conventional way (Kristensen et al., 2008), marking the location of 68 landmarks on the cranium and 17 on the mandible (Supplementary Fig. 1). Crania and mandibles were analysed separately since their relative position varied from subject to subject. Landmarks for all crania and mandibles were aligned using Procrustes Superimposition, and these data were used for further statistical analysis of size and shape.

For the landmark-free approach we developed a pipeline based on previous approaches in morphometrics and neuroimaging (Fig. 1, Table 1, Supplementary Appendix 1). In brief, following thresholding to extract the skull structures from the μCT images, cartilaginous structures were removed (Supplementary Fig. 2) and the images segmented using bone density to separate the mandibles from the crania (step 1). Triangulated meshes were generated from the surfaces (including internal surfaces) of the cranium and mandible for all subjects (step 2), aligned (and scaled where appropriate – see below) (step 3). The meshes were used for the construction of an atlas (mean shape) for the crania and mandibles of the

122 WT and Dp1Tyb skulls (step 4). Atlas construction was based on the Deformetrica algorithm
123 (Durrleman et al., 2014) which works by defining a flow field (tensor) that conforms to its shape
124 and quantifies deformations from it to each subject recorded as momentum vectors (momenta
125 - see Methods and Supplementary Appendix 1). The initial output from this atlas consisted of
126 the average mesh for the whole population (based on averaging the tensors), a set of control
127 points corresponding to areas with the greatest variability between subjects, and momenta for
128 each control point describing the directional variation of the shape from the average. The
129 average mesh, the control points and the momenta were used for further statistical analysis,
130 with the momenta applied to deform the population average mesh to generate average
131 meshes for each of WT and Dp1Tyb groups preserving one-to-one correspondence of mesh
132 vertices. We performed principal component analysis and used a multiple permutations test
133 on a stratified k-fold cross validation classifier to test for significance (step 5). To control for
134 overfitting (a risk when the number of measurements substantially exceeds the number of
135 subjects), we compared the PCA difference vector magnitude between the two genotype
136 groups with that of 1000 randomly scrambled groups. We found that the distribution was
137 Normal and that the genotype difference vector was more than 3.5 standard deviations away
138 from the mean vector of the 1000 scrambled groups for both cranium and mandible, thus
139 showing that overfitting is unlikely to be a significant factor (data not shown).
140

141 **Size differences: Dp1Tyb mice have significantly smaller crania and mandibles**

142 We used centroid size (the mean absolute landmark distance from the landmark-defined
143 centroid) to compare overall sizes of Dp1Tyb and sibling control specimens (Klingenberg,
144 2016). Landmark-based centroid size comparison showed that the crania and mandibles of
145 Dp1Tyb mice were both significantly smaller than those of WT mice (Fig. 2A, C), recapitulating
146 the overall reduction in skull size found in humans with DS and as well as in other models of
147 DS (Hill et al., 2007; Richtsmeier et al., 2000; Richtsmeier et al., 2002; Starbuck et al., 2014;
148 Suri et al., 2010). The landmark-free analysis also showed that Dp1Tyb crania and mandibles
149 were significantly smaller (Fig. 2B, D). Both methods showed an approximately 7% reduction

150 in centroid size of both cranium and mandible in Dp1Tyb mice (Supplementary Table). The
151 landmark-free and landmark-based centroid sizes were different in absolute magnitude,
152 unsurprisingly given the many extra measurements use in the landmark-free method (~19,000
153 mesh vertices versus 68 landmarks for cranium and ~16,000 vertices versus 17 landmarks for
154 mandible).
155
156 **Shape differences: Dp1Tyb mice have altered crania and mandibles**
157 Both the size difference and gross shape differences were clearly visualised by animated
158 morphing between the mean shapes of WT and Dp1Tyb specimens (generated in the
159 landmark-free pipeline) for the cranium and the mandible (Supplementary Videos 1, 2). The
160 overall decrease in size going from WT to Dp1Tyb crania or mandibles was readily apparent
161 and some shape changes could also be seen, although the latter were more subtle.
162
163 To quantify shape differences statistically, shape was separated from size by scaling the data
164 to equalise centroid sizes (Procrustes alignment). To analyse residual shape differences
165 between genotypes, we used principal component analysis (PCA). Both landmark-based and
166 landmark-free methods showed a statistically significant differences in shape between
167 Dp1Tyb and WT mice in both crania and mandibles (Fig. 2E-H). Plots of the first two Principal
168 Components identified by the two different methods looked similar, with tighter clustering of
169 specimens for cranium than for mandible.
170
171 **Shape difference localisation: Dp1Tyb mice recapitulate aspects of human DS**
172 **craniofacial dysmorphology**
173 To characterise the shape differences anatomically, we first, simply overlaid the mean
174 landmark configurations from Dp1Tyb and WT crania and mandibles (Fig. 3A-F). Second, we
175 applied an established thin-plate spline interpolation and comparison package (Morpho R -
176 see Methods) to the landmark data to generate displacement heatmaps (Fig. 3G-L). Direct
177 inspection revealed that the morphological differences between Dp1Tyb and WT skulls were

178 broadly distributed and relatively subtle, consistent both with previously reported mouse DS
179 models and with the human phenotype (Fischer-Brandies, 1988; Fischer-Brandies et al., 1986;
180 Suri et al., 2010). The maps revealed that Dp1Tyb mice have a more domed neurocranium
181 (cyan points at the top-right of Fig. 3A, dark red regions in Fig. 3G, H, J). The cranial doming
182 in combination with the overall smaller size compared to WT mice constitute a net
183 anteroposterior shortening in Dp1Tyb mice, i.e. brachycephaly, a predominant feature of the
184 human DS phenotype. This method also indicated an almost unchanged cranial base (Fig. 3I)
185 and some contraction (anterior movement) concentrated around the magnum foramen in the
186 occipital bone of Dp1Tyb crania (points at right of Fig. 3C, blue colour on the right of Fig. 3I
187 and in Fig. 3J). These maps also showed a smaller snout in Dp1Tyb mice as a result of a
188 reduction in size of the nasal bones (Fig. 3G, H). Although not evident in the heatmaps, the
189 Dp1Tyb cranium was wider as can be seen by the displacement of the zygomatic processes'
190 landmarks laterally (Fig. 3C and D). The reduced snout and facial widening in combination
191 with the overall smaller size of the Dp1Tyb crania mimics the "mid-face hypoplasia" of human
192 DS. The Dp1Tyb mandibles had a small shape change in the alveolar ramus region and the
193 condylar process but these mandibular changes were all extremely subtle (Fig. 3E, F, K, L).
194
195 Next we made heatmaps based on the higher-resolution landmark-free method. Displacement
196 maps together with the morphing movies visualised the distances between the two mean
197 meshes. We plotted net displacement rather than movement towards or away from the shape
198 centroid so that only one colour was needed in the maps, using videos to show the direction
199 of differences. The landmark-free analysis showed changes mostly similar to those found
200 using the landmark-based method including the same relative doming of the neurocranium,
201 and shortening of the nasal and maxillary processes (Fig. 4A-D, Supplementary Video 3).
202
203 Differences between Dp1Tyb and WT mandibles were overall much more subtle (Fig. 4E,F,
204 Supplementary Video 4) consisting of a few tens of microns only. Re-scaling the heatmap
205 colour range better visualised the localisation of the differences (Fig. 4G,H) as did generating

a video in which the shape change of the mandible was exaggerated by a factor of three (Supplementary Video 5). Thus, we see the expansion buccally (cheek-wards) of the inferior portion of the ramus (the region just posterior to the molars), the contraction of the angular process, lingual movement of the molar ridge and widening of the incisor alveolus. The expansion of the ramus had not shown up in the landmark-based method because there were no landmarks in this region.

New shape change information: The landmark-free method maps in-plane deformation

One of the reasons for separating shape difference from size difference in morphometrics is that a simple uniform scale change would appear, artefactually, as change localised distal to whatever point was used as the common frame of reference (i.e. if the centroids are used, there is an increasing centre-to-edge gradient – see demonstration in Suppl. Fig.3). Scaling avoids this problem, but throws away the "ground truth" of the differences. One solution is to find a way of showing size changes entirely locally, capturing surface "stretch" as a measure of local growth differences between specimens. This is also likely to reflect real biological differences which arise in development due to different localised growth. This is not possible with landmarks, but can be done within the high-resolution landmark-free method where a high density of control points is used to guide an even higher density of mesh vertices. Thus, we calculated and mapped local differences in mesh vertex spacing. We used the spacing to generate a heat map without the need for scaling. The results are shown in Fig.5A-F and Supplementary Videos 1, 2 and 6 (see also Supplementary Video 10 for another way of displaying the data). These maps clearly show that the phenotype is almost entirely a growth deficit in the occipital region, posterior of the auditory bulla, facial bones and hard palate. Expansion in the mid-cranial vault is minimal. This representation can be compared with the heatmaps generated on size-scaled data (Fig.5G-L and Supplementary Videos 8 and 9): in these the colour emphasises the expansion of the cranial vault, but this is a relative rather than absolute expansion and does not correspond to actual growth.

Discussion

In this paper, we have presented an adaptation and incorporation of a tensor field-based landmark-free shape comparison methodology (Durrleman et al., 2014) into a pipeline that can compare shapes and provide statistical and other data analyses comparable to more traditional geometric morphometrics but with less need for expert training, less labour, less chance of operator error and a higher spatial resolution. We used this pipeline to analyse the previously unexamined craniofacial phenotype of Dp1Tyb mice, a relatively new model of DS (Lana-Elola et al., 2016) and identified localised differences more precisely than was previously possible. The high resolution enabled local deformation density mapping which bypasses some of the issues around global scaling for shape comparison and enabled mapping of the dysmorphology specifically to the occipital and naso-palatal regions.

Both methods revealed that Dp1Tyb mice have size and shape differences compared to WT that parallel the DS phenotype in previously described DS mouse models and in humans. Both separated Dp1Tyb from WT in shape space using one or two principal components and both revealed the significantly reduced size of the cranium and mandible of Dp1Tyb mice, and more specifically, both described brachycephaly (shortened head), resolved in the analysis to an overall size reduction plus cranial doming.

Nonetheless, the landmark-free method has clear advantages. Methodologically, there are three. First is consistency: the landmark-free method overcomes the limitations of manual placement of landmarks which is susceptible to inter- and intra-operator error (Robinson and Terhune, 2017). Second is labour saving: although the landmark-free method requires some manual input in the early stages, particularly in determining image thresholding and in cleaning up imperfect anatomical segmentation, it is substantially less labour-intensive and requires less user training than the landmark-based approach. Third, and perhaps most scientifically significant, is resolution: the landmark-free method provides much higher resolution and

information density than the landmark-based method. In principle, the landmark-free method offers arbitrarily high resolution. In practice we found that decimating the initial mesh from ~2,800,000 to ~19,000 vertices for the cranium (~200,000 to ~16,000 for the mandible) and using a kernel size in the Deformetrica algorithm of 1mm to yield ~ 2500 control points for the cranium (~700 for the mandible) captured the interesting anatomical features at high density while avoiding noise, e.g. trivial surface texture differences. Different sizes of specimen will have different optimal spatial parameters. The high density of control points was further refined by having them clustered algorithmically at regions of high variability between samples. This might be contrasted with the inherent bias in landmarking that tends to place shape differences close to landmarks (observable in, for example, Fig. 3A, B). It can also be contrasted with the use of semi-landmarks, which adds landmarks that are evenly distributed across contours or surfaces that are bounded by identifiable landmarks (Adams and Collyer, 2018; Gunz et al., 2005) but still potentially leaves gaps where landmarks are sparse. A trade-off for all methods that increase the number of discrete observations, however, is the increasing as risk of overfitting as the number of variables (e.g. landmarks or voxels) increases relative to the statistical degrees of freedom, or the “curse of dimensionality” (Indyk and Motwani, 1998). Controls for overfitting, such as the permutation test we applied, are therefore essential.

Is the higher resolution and more complete coverage useful? We found that the landmark-free approach allowed us to see changes not visible using the landmark-based approach. Most strikingly, we were able to observe a shape difference in the lower-posterior mandible, where landmarks are absent, and in the snout and palate, where landmarks are more abundant but possibly not dense enough to capture the localised in-plane differences. These latter changes in particular indicate homology with the mid-face hypoplasia found in humans with DS. This will be useful in understanding how DS genes result in dysmorphology because we now have a better knowledge of their location of action.

288 At another level, high resolution is useful because it enables mapping of surface "stretch" by
289 retaining all the vertices of the mesh, in effect making each vertex a landmark. The very short
290 spatial scale of this mapping is likely to be a much better way to capture and localise changes
291 in biologically causal processes, such as cell proliferation or extracellular matrix expansion,
292 compared to net displacement, where the cause could be hundreds of cell diameters away.
293 The local nature of this deformation mapping makes it easier to interpret the visual display of
294 the deformations without global scaling.
295
296 Although the landmark-free method was developed for MRI scans of brains[24] applying it to a
297 mutant skull has enabled two important conclusions. The first is that using a landmark-free
298 approach is still advantageous even when traditional landmarking is possible. The second
299 conclusion is that it is possible to apply this approach in the form of a relatively user-friendly
300 tool. We have found it useful in understanding the DS craniofacial phenotype but, with modest
301 computational expertise, other researchers can tackle any mutant phenotype, including where
302 traditional methods have struggled, such as in early developmental stages or other biological
303 forms that lack well defined landmarks.
304

305 Materials and Methods

306 Mice and imaging

307 C57BL/6J.129P2-Dp(16Lipi-Zbtb21)1TybEmcf (Dp1Tyb) mice (Lana-Elola et al., 2016) were
308 bred at the MRC Harwell Institute. All mice were backcrossed to C57BL/6JNimr for at least 10
309 generations. All animal work was approved by the Ethical Review panel of the Francis Crick
310 Institute and was carried out under Project Licences granted by the UK Home Office. Heads
311 from 20 mice at 16 weeks of age were used (10 Dp1Tyb and 10 WT, 5 male and 5 female of
312 each genotype). However, 4 subjects were excluded from the analysis due to fractures in
313 either the mandible or skull. Heads were prepared for micro-computed tomography (µCT) by
314 fixation in PFA and then scanned at a 25 µm resolution using a µCT 50 (Scanco).

315

316 **Landmark-based morphometric analysis**

317 *Landmark Acquisition*

318 Three-dimensional locations of 68 anatomical landmarks for the cranium and 17 landmarks
319 for the mandible (Supplementary Fig. 1) as previously defined by Hallgrimsson and colleagues
320 (Hallgrimsson et al., 2007) were placed onto 3D reconstructions of µCT images using
321 Microview (Parallax Innovations). Landmarks were placed manually and verified by checking
322 orthogonal planar views of the subject.

323

324 *Statistical analysis of landmark dataset*

325 Landmarks for all subjects were aligned using Procrustes superimposition, and distances
326 between landmarks for each subject were analysed by Principal Component Analysis (PCA)
327 using MorphoJ (Klingenberg, 2011) to visualise group separation by shape. To quantify
328 significance in shape differences between genotypes we used the Procrustes Distance
329 Multiple Permutations test (1000 iterations) within MorphoJ. Centroid size was calculated as
330 the square root of the sum of the squared distances from each landmark to the centroid i.e.
331 the centre of mass of all landmarks of a given specimen and was used to compare size
332 differences between WT and Dp1Tyb crania and mandibles. The statistical significance of
333 such size differences was calculated using a 2-tailed unpaired t-test.

334

335 Shape changes after Procrustes scaling were visualised as heatmaps. Using the Morpho R
336 package function tps3d (documentation for which can be found at
337 https://www.rdocumentation.org/packages/Morpho/versions/2.6/topics/tps3d), mean
338 landmark sets of each genotype group were used to interpolate an average mesh, using a
339 thin-plate spline method (Bookstein, 1989), thus providing a mesh for both the mean WT
340 shape and mean Dp1Tyb shape. The Morpho R meshdist function
341 (https://www.rdocumentation.org/packages/Morpho/versions/2.6/topics/meshDist) was then
342 used to create the heatmaps. The function first calculates the distances of the reference

meshes vertices (in this case mean WT mesh) to that of the target mesh (mean Dp1Tyb mesh). Then, using a previously proposed algorithm (Baerentzen, 2005), the distances were given a negative value if inside the reference mesh or a positive value if outside. A vector containing blue and red colour values was assigned to the negative and positive values respectively (Schlager, 2017).

Landmark-free morphometric analysis

As an alternative to landmark population comparisons, statistical analysis of anatomical shapes can be achieved using so-called atlas-based approaches, which consist of estimating an anatomical model (i.e. template) as the mean of a set of input shapes (rather than point clouds) and quantifying its variation in a test population as deformations. This was previously achieved in a reproducible and robust landmark-free manner by Durrleman et al (2014). This approach bypasses a number of problems associated with mesh point-to-point comparison by representing deformation between shapes as the diffeomorphic transformation of flow fields, i.e. currents over the mesh surface. Currents are parameterised by a set of control points in space and initial velocities, or momenta. By means of a gradient descent optimisation scheme, the method is able to produce a statistical atlas of the population of shapes. An atlas refers to a mean template shape, a set of final control point positions, and momenta parameterising the displacements between the template to each initial individual shape. In the following sections we describe the different steps to achieve such analysis.

Landmark-free Atlas Construction

Step 1 (Fig. 1, Table 1, Supplementary Appendix 1). Despite the fact that images acquired using µCT show good bone contrast, they often include the presence of artificial objects (noise and debris in the specimen), small holes and cartilage that need be excluded in order to obtain consistently comparable final surface meshes. To extract the surface meshes, a series of image processing steps were applied. After a thresholding operation to extract the skull, "morphological opening" and "closing" were performed on the binary mask to remove internal

371 cartilage structures (Supplementary Fig. 2). Removal of spurious objects was achieved by
372 clustering, categorising all of the connected components in an image by size and retaining
373 only the largest component. Skulls were segmented using bone density to isolate the mandible
374 (whose density is higher than that in the rest of the skull). However, this segmentation of the
375 mandible can happen improperly and may include parts of the temporal bone which must be
376 cleaned and removed manually. Mandible meshes were extracted from the skull binary mask
377 semi-automatically using Watershed segmentation (Mangan and Whitaker, 1999).
378
379 Step 2. The meshes were produced using marching cubes on the binary images, followed by
380 a surface Laplacian smoothing (Vollmer et al., 1999) and finally decimation of a factor of 1/80
381 to decrease mesh resolution and reduce overall computation time.
382
383 Step 3. The atlas construction necessitates the production of aligned meshes from the input
384 μCT images as a pre-processing step. Minimally 3 pairs of landmarks were chosen to align
385 meshes using a Procrustes technique (Gower, 1975) using a rigid body-plus-scaling
386 transformation model (similarity alignment) or a rigid body transformation without scaling (rigid
387 body alignment).
388
389 Step 4. As previously described (Durrleman et al., 2014), the atlas construction major hyper-
390 parameters consist of (1) the size of the Gaussian kernel used to represent shapes in the
391 varifold of currents, denoted σ_W, and (2) the number of control points, denoted N_{cp}. Control
392 points can be thought of as unbiased landmarks, initially they are spaced on a regular grid
393 evenly but move to areas of greatest variation. Thus as much as possible of the shape change
394 is captured in an unbiased manner. σ_W can be seen as the precision at which the shape
395 deformation is described. N_{cp} denotes the sampling density in space. In our experiments, we
396 fixed σ_W = 2 mm. Using that scale, the derived number of control points Ncp was 350 and 940
397 for the mandibles and the cranium analyses respectively. All subjects' meshes were used for
398 the construction of the atlas. The optimisation procedure typically converged within 150

iterations in approximately 20h on a 10 core cpu for the mandible. The atlas construction produces the following outputs:

- **Control Points**: For each subject, the N_{cp} final control points locations {c}, that correspond to areas that describe the population's most important variability in shape.
- **Momenta**: For each subject, the N_{cp} final momenta {m} associated to each control point, that describe the shape directional variation from the population average.
- **Template**: Mean shape of the population.

Landmark-free dataset statistical analysis

Step 5 (Fig. 1). The atlas outputs provide a dense amount of information that can be used for various statistical analyses. Centroid size was calculated as the square root of the sum of the squared distances from each mesh node to the centroid of all nodes of a given specimen. Non-linear Kernel PCA with dimension 5 was applied to the set of momenta produced from the atlas of the population, in order to find the principal modes of variation of the entire population. The resulting output provided a way to compare these results with the landmark-based PCA analysis. We projected the subjects onto the feature space for comparison purposes. Such projection provides dense information of shape differences between the two sub-populations. Local magnitude of the momenta interpolated at the template mean mandible (or cranium) mesh point locations allow for additional qualitative interpretation of shape differences between groups. Stratified k-fold cross-validation analysis was performed on the PCA data to evaluate the statistical power of classification between the two groups. Significance of the classification score was tested using a multiple permutations test at 1000 iterations (Ojala and Garriga, 2010). To assess overfitting, subjects were randomly partitioned into two groups ("scrambled groups") and PCA analysis performed to generate inter-group vectors. The distribution of the vector magnitudes was tested for Normality using the Shapiro-Wilk test.

425 **Code availability**

426 Python scripts and documentation for the landmark-free morphometric analysis are freely
427 available on GitHub (https://gitlab.com/ntoussaint/landmark-free-morphometry) and their use
428 is also described in Supplementary Appendix 1.

429

430 **Acknowledgements**

431 We thank Heather Cater and Sara Wells from MRC Harwell for breeding the mice and Chris
432 Healy at KCL for performing the micro-CT scans.

433

434 **Author contributions**

435 NT designed and wrote the code for the analysis. YR and WL carried out experiments. NT,
436 YR and WL analysed the data. YR, NT, VLJT, JAS and JBAG wrote paper. BH, EMCF, VLJT,
437 JBAG and JAS supervised the work.

438

439 **Competing interests**

440 The authors declare no competing interests.

441

442 **Funding**

443 VLJT and EMCF are supported by the Wellcome Trust (grants 080174, 098327 and 098328)
444 and VLJT by the Francis Crick Institute which receives its core funding from Cancer Research
445 UK (FC001194), the UK Medical Research Council (FC001194), and the Wellcome Trust
446 (FC001194). YR was supported by the Francis Crick Institute and King's College London.
447 JBAG was supported by King's College London. NT and JAS acknowledge support from the
448 Wellcome/EPSRC Centre for Medical Engineering [WT 203148/Z/16/Z] and the Wellcome
449 Trust IEH Award [102431]. BH is supported by a CIHR Foundation grant, NIH R01
450 R01DE019638 and the Canadian Foundation for Innovation.

References

Adams, D. C. and Collyer, M. L. (2018). Multivariate Phylogenetic Comparative Methods: Evaluations, Comparisons, and Recommendations. *Syst Biol* **67**, 14-31.

Andresen, P. R., Bookstein, F. L., Conradsen, K., Ersboll, B. K., Marsh, J. L. and Kreiborg, S. (2000). Surface-bounded growth modeling applied to human mandibles. *IEEE Trans Med Imaging* **19**, 1053-1063.

Antonarakis, S. E. (2017). Down syndrome and the complexity of genome dosage imbalance. *Nat Rev Genet* **18**, 147-163.

Baerentzen, J. A. (2005). Robust generation of signed distance fields from triangle meshes. *Volume Graphics 2005*, 167-+.

Bookstein, F. L. (1989). Principal Warps - Thin-Plate Splines and the Decomposition of Deformations. *Ieee T Pattern Anal* **11**, 567-585.

---- (1997). Landmark methods for forms without landmarks: morphometrics of group differences in outline shape. *Med Image Anal* **1**, 225-243.

Bron, E. E., Smits, M., van der Flier, W. M., Vrenken, H., Barkhof, F., Scheltens, P., Papma, J. M., Steketee, R. M., Mendez Orellana, C., Meijboom, R., et al. (2015). Standardized evaluation of algorithms for computer-aided diagnosis of dementia based on structural MRI: the CADDementia challenge. *Neuroimage* **111**, 562-579.

Cooke, S. B. and Terhune, C. E. (2015). Form, function, and geometric morphometrics. *Anat Rec (Hoboken)* **298**, 5-28.

Durrleman, S., Prastawa, M., Charon, N., Korenberg, J. R., Joshi, S., Gerig, G. and Trouve, A. (2014). Morphometry of anatomical shape complexes with dense deformations and sparse parameters. *Neuroimage* **101**, 35-49.

Fischer-Brandies, H. (1988). Cephalometric comparison between children with and without Down's syndrome. *Eur J Orthod* **10**, 255-263.

Fischer-Brandies, H., Schmid, R. G. and Fischer-Brandies, E. (1986). Craniofacial development in patients with Down's syndrome from birth to 14 years of age. *Eur J Orthod* **8**, 35-42.

Frangi, A. F., Rueckert, D., Schnabel, J. A. and Niessen, W. J. (2003). Automatic Construction of Biventricular Statistical Shape Models. In *Functional Imaging and Modeling of the Heart* (eds I. E. Magnin, J. Montagnat, P. Clarysse, J. Nenonen & T. Katila), pp. 18-29. Berlin, Heidelberg: Springer Berlin Heidelberg.

Gori, P., Colliot, O., Marrakchi-Kacem, L., Worbe, Y., Poupon, C., Hartmann, A., Ayache, N. and Durrleman, S. (2017). A Bayesian framework for joint morphometry of surface and curve meshes in multi-object complexes. *Med Image Anal* **35**, 458-474.

Gower, J. C. (1975). Generalized Procrustes Analysis. *Psychometrika* **40**, 33-51.

Gunz, P., Mitteroecker, P. and Bookstein, F. L. (2005). Semilandmarks in Three Dimensions. In *Modern Morphometrics in Physical Anthropology* (ed. D. E. Slice), pp. 73–98. New York: Kluwer Academic Publishers-Plenum Publishers.

Hallgrimsson, B., Lieberman, D. E., Liu, W., Ford-Hutchinson, A. F. and Jirik, F. R. (2007). Epigenetic interactions and the structure of phenotypic variation in the cranium. *Evol Dev* **9**, 76-91.

Herault, Y., Delabar, J. M., Fisher, E. M. C., Tybulewicz, V. L. J., Yu, E. and Brault, V. (2017). Rodent models in Down syndrome research: impact and future opportunities. *Dis Model Mech* **10**, 1165-1186.

Hill, C. A., Reeves, R. H. and Richtsmeier, J. T. (2007). Effects of aneuploidy on skull growth in a mouse model of Down syndrome. *J Anat* **210**, 394-405.

Indyk, P. and Motwani, R. (1998). Approximate nearest neighbors: towards removing the curse of dimensionality. In *Proceedings of the thirtieth annual ACM symposium on Theory of computing*, pp. 604-613. Dallas, Texas, USA: ACM.

Jenkinson, M., Beckmann, C. F., Behrens, T. E. J., Woolrich, M. W. and Smith, S. M. (2012). FSL. *NeuroImage* **62**, 782-790.

Klingenberg, C. P. (2011). MorphoJ: an integrated software package for geometric morphometrics. *Mol Ecol Resour* **11**, 353-357.

---- (2016). Size, shape, and form: concepts of allometry in geometric morphometrics. *Dev Genes Evol* **226**, 113-137.

Korenberg, J. R., Chen, X. N., Schipper, R., Sun, Z., Gonsky, R., Gerwehr, S., Carpenter, N., Daumer, C., Dignan, P., Disteche, C., et al. (1994). Down-Syndrome Phenotypes - the Consequences of Chromosomal Imbalance (Vol 91, Pg 4997, 1994). *P Natl Acad Sci USA* **91**, 11281-11281.

Kristensen, E., Parsons, T. E., Hallgrimsson, B. and Boyd, S. K. (2008). A novel 3-D image-based morphological method for phenotypic analysis. *IEEE Trans Biomed Eng* **55**, 2826-2831.

Lana-Elola, E., Watson-Scales, S., Slender, A., Gibbins, D., Martineau, A., Douglas, C., Mohun, T., Fisher, E. M. and Tybulewicz, V. (2016). Genetic dissection of Down syndrome-associated congenital heart defects using a new mouse mapping panel. *Elife* **5**.

Lana-Elola, E., Watson-Scales, S. D., Fisher, E. M. and Tybulewicz, V. L. (2011). Down syndrome: searching for the genetic culprits. *Dis Model Mech* **4**, 586-595.

Lejeune, J., Gautier, M. and Turpin, R. (1959). [Study of somatic chromosomes from 9 mongoloid children]. *C R Hebd Seances Acad Sci* **248**, 1721-1722.

Mangan, A. P. and Whitaker, R. T. (1999). Partitioning 3D surface meshes using watershed segmentation. *Ieee T Vis Comput Gr* **5**, 308-321.

Nolden, M., Zelzer, S., Seitel, A., Wald, D., Muller, M., Franz, A. M., Maleike, D., Fangerau, M., Baumhauer, M., Maier-Hein, L., et al. (2013). The Medical Imaging Interaction Toolkit: challenges and advances : 10 years of open-source development. *Int J Comput Assist Radiol Surg* **8**, 607-620.

Ojala, M. and Garriga, G. C. (2010). Permutation Tests for Studying Classifier Performance. *J. Mach. Learn. Res.* **11**, 1833-1863.

Palci, A. and Lee, M. S. Y. (2019). Geometric morphometrics, homology and cladistics: review and recommendations. *Cladistics* **35**, 230-242.

Pedregosa, F., Varoquaux, G., Gramfort, A., Michel, V., Thirion, B., Grisel, O., Blondel, M., Prettenhofer, P., Weiss, R., Dubourg, V., et al. (2011). Scikit-learn: Machine Learning in Python. *J Mach Learn Res* **12**, 2825-2830.

Percival, C. J., Green, R., Marcucio, R. and Hallgrimsson, B. (2014). Surface landmark quantification of embryonic mouse craniofacial morphogenesis. *Bmc Dev Biol* **14**.

Richtsmeier, J. T., Baxter, L. L. and Reeves, R. H. (2000). Parallels of craniofacial maldevelopment in Down syndrome and Ts65Dn mice. *Dev Dyn* **217**, 137-145.

Richtsmeier, J. T., Zumwalt, A., Carlson, E. J., Epstein, C. J. and Reeves, R. H. (2002). Craniofacial phenotypes in segmentally trisomic mouse models for Down syndrome. *Am J Med Genet* **107**, 317-324.

Robinson, C. and Terhune, C. E. (2017). Error in geometric morphometric data collection: Combining data from multiple sources. *Am J Phys Anthropol* **164**, 62-75.

Routier, A., Gori, P., GracianoFouquier, A. B., Lecomte, S., Colliot, O. and Durrleman, S. (2014). Evaluation of morphometric descriptors of deep brain structures for the automatic classification of patients with Alzheimer's disease, mild cognitive impairment and elderly controls. In *Proc MICCAI Work. Chall. Comput. Diagnosis Dement. Based Struct. MRI Data*, pp. pp.74-81. Cambridge, MA, USA.

Schlager, S. (2017). Chapter 9 - Morpho and Rvcg – Shape Analysis in R: R-Packages for Geometric Morphometrics, Shape Analysis and Surface Manipulations. In *Statistical Shape and Deformation Analysis* (ed. G. Zheng, S. Li & G. Székely), pp. 217-256: Academic Press.

Schroeder, W., Martin, K. M. and Lorensen, W. E. (1998). *The visualization toolkit (2nd ed.): an object-oriented approach to 3D graphics*. Upper Saddle River, NJ, USA: Prentice-Hall, Inc.

Shearer, B. M., Cooke, S. B., Halenar, L. B., Reber, S. L., Plummer, J. E., Delson, E. and Tallman, M. (2017). Evaluating causes of error in landmark-based data collection using scanners. *Plos One* **12**.

Starbuck, J. M., Dutka, T., Ratliff, T. S., Reeves, R. H. and Richtsmeier, J. T. (2014). Overlapping trisomies for human chromosome 21 orthologs produce similar effects on skull and brain morphology of Dp(16)1Yey and Ts65Dn mice. *Am J Med Genet A* **164A**, 1981-1990.

Suri, S., Tompson, B. D. and Cornfoot, L. (2010). Cranial base, maxillary and mandibular morphology in Down syndrome. *Angle Orthod* **80**, 861-869.

Vollmer, J., Mencl, R. and Muller, H. (1999). Improved laplacian smoothing of noisy surface meshes. *Comput Graph Forum* **18**, C131-C138.

von Cramon-Taubadel, N., Frazier, B. C. and Lahr, M. M. (2007). The problem of assessing landmark error in geometric morphometrics: Theory, methods, and modifications. *Am J Phys Anthropol* **134**, 24-35.

Watson-Scales, S., Kalmar, B., Lana-Elola, E., Gibbins, D., La Russa, F., Wiseman, F., Williamson, M., Saccon, R., Slender, A., Olerinyova, A., et al. (2018). Analysis of motor dysfunction in Down Syndrome reveals motor neuron degeneration. *PLoS Genet* **14**, e1007383.

Webster, M. and Sheets, H. D. (2010). A Practical Introduction to Landmark-Based Geometric Morphometrics. *The Paleontological Society Papers* **16**, 163-188.

Yaniv, Z., Lowekamp, B. C., Johnson, H. J. and Beare, R. (2018). SimpleITK Image-Analysis Notebooks: a Collaborative Environment for Education and Reproducible Research. *Journal of Digital Imaging* **31**, 290-303.

Yu, T., Li, Z., Jia, Z., Clapcote, S. J., Liu, C., Li, S., Asrar, S., Pao, A., Chen, R., Fan, N., et al. (2010). A mouse model of Down syndrome trisomic for all human chromosome 21 syntenic regions. *Hum Mol Genet* **19**, 2780-2791.

Step	Sub-step	Function	Parameters	Tool	Reference
Step 1. Pre-processing	Binary segmentation	Binary threshold	threshold = 10000	FSL	(Jenkinson et al., 2012)
		Closing	kernel size = 5		
		Opening	kernel size = 3		
		Clustering and extraction of largest component			
		Fill holes			
	Object parcelation	Watershed	watershedlevel = 0.22	SimpleITK	(Yaniv et al., 2018)
Step 2. Mesh extraction	Mesh extraction	Marching cubes		VTK	(Schroeder et al., 1998)
		Smoothing	number of iterations = 20 relaxation factor = 0.6		
Step 3. Mesh Alignment	Alignment points	Reference points used to align meshes		MITK	(Nolden et al., 2013)
	Mesh Alignment	Centroid size		VTK/Numpy	
		vtkProcrustesAlignmentFilter	Rigid body or similarity	VTK	
Step 4. Atlas	Atlas construction	Atlas construction	data-sigma = 10 kernel width (template) = 2.5mm kernel width (subject) = 2mm number of time points = 10 max iterations = 150 number of threads = 19	Deformetrica	(Gori et al., 2017)
Step 5. Statistical analysis	Principal component analysis	Kernel PCA	number of components = 5	Scikit-learn	(Pedregosa et al., 2011)
		Kernel PCA lambdas (eigen values)			
		Support vector machine			
		Permutation test			
		Cross validation			
	Momenta projection / morph	Shooting	template kernel width = 2.0 deformation kernel width = 1.5	Deformetrica	

Table 1. Summary of steps in the landmark-free analysis pipeline and chosen parameters at each step.

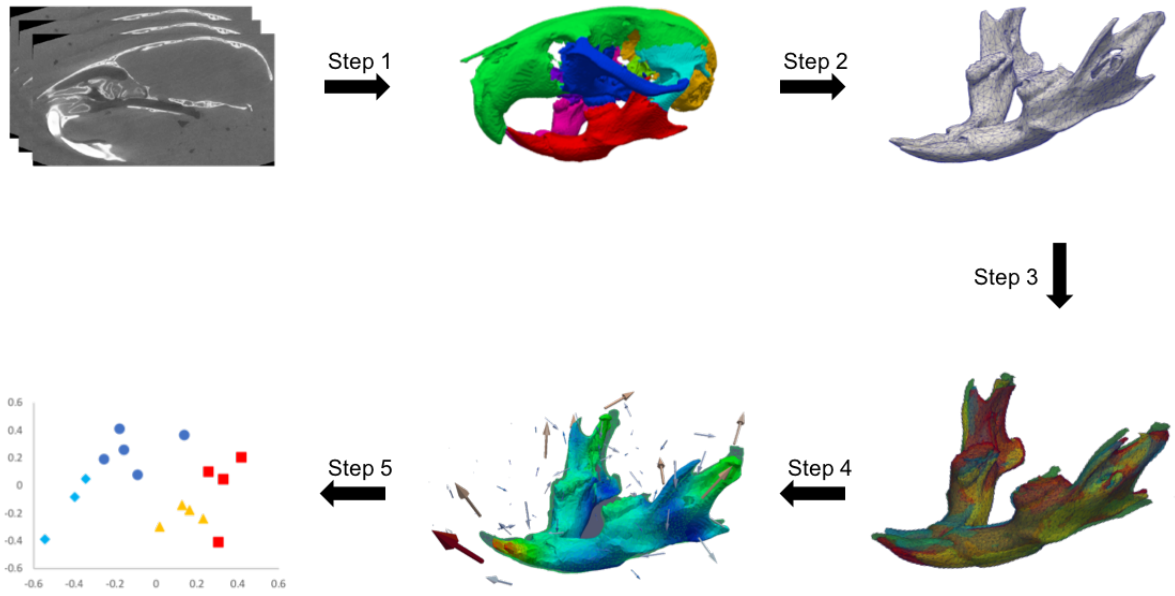

Figure 1. Stages of processing in the landmark-free approach. Step 1, extraction of region of interest. Initial thresholding of μCT image was used to make a binary mask and regions of the mask were separated by bone density using secondary thresholding, with some manual clean-up based on known anatomy. A region of interest (in this example the mandible in red) was chosen for further analysis. Step 2, mesh generated and decimated by a factor of 0.0125 to reduce data file size. Step 3, meshes of all subjects aligned either using rigid body alignment with no scaling or similarity alignment with scaling. Step 4, atlas construction. Step 5, statistical analysis and visualisation of shape data.

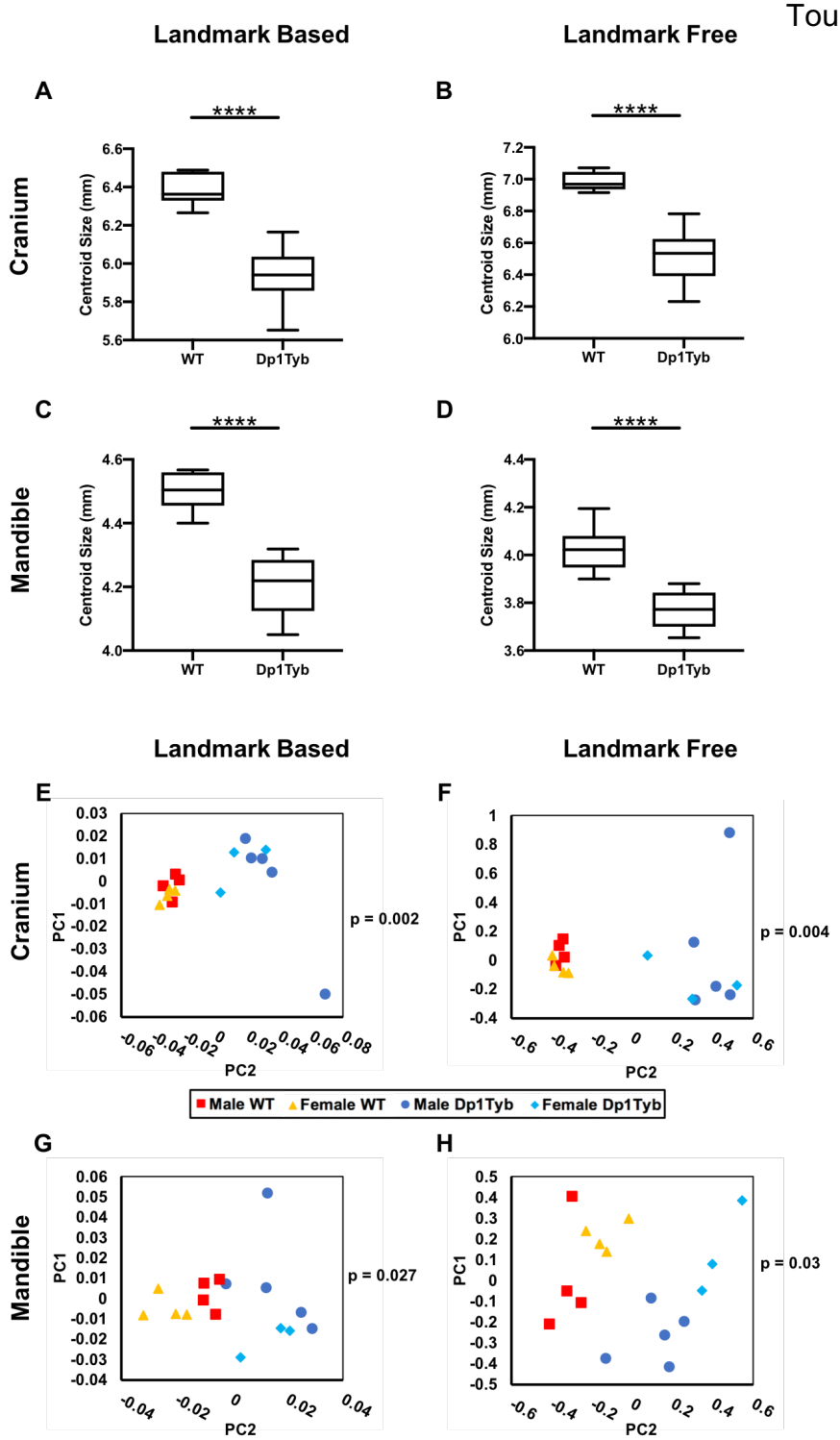

Figure 2. Decreased size and altered shape of Dp1Tyb crania and mandibles. A-D Centroid sizes of WT and Dp1Tyb crania (**A, B**) and mandibles (**C, D**) determined using landmark-based (**A, C**) and landmark-free (**B, D**) methods. Data shown as box and whiskers plots indicating the 25% and 75% centiles (box), range of all data points (whiskers) and the median (black line). Statistical significance was calculated using a two-tailed unpaired t-test; **** $P < 0.0001$. **E-H** Principal component analysis (first two components) of Procrustes aligned shapes of WT and Dp1Tyb crania (**E, F**) and mandibles (**G, H**) determined using landmark-based (**E, G**) and landmark-free (**F, H**) methods. Statistical significance of the differences between the WT and Dp1pTyb groups of samples was calculated using a permutation test, and *P*-values are shown on the plots. Sample size: n = 8 of each genotype.

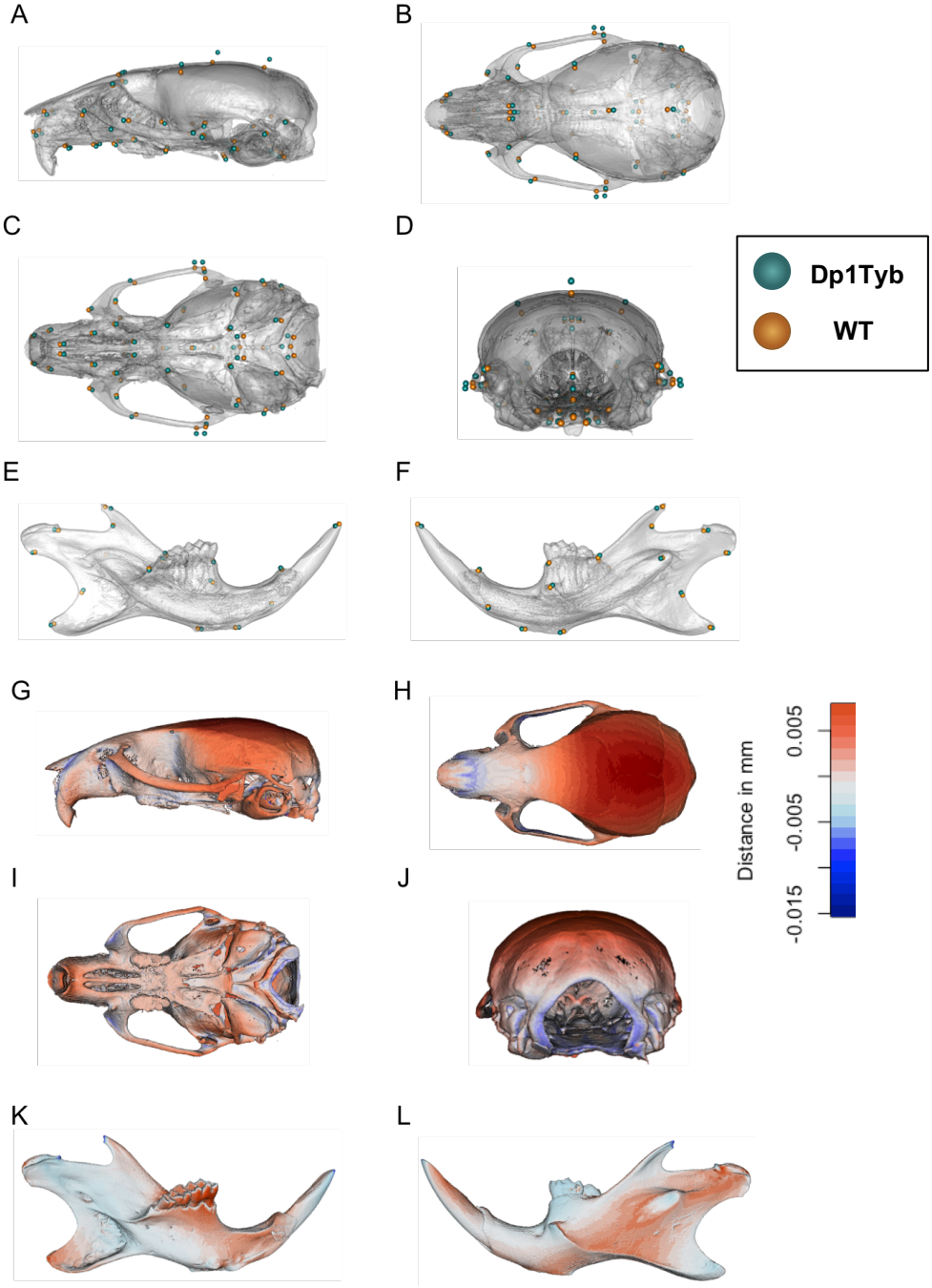

Figure 3. Visualisation of altered shape of Dp1Tyb crania and mandibles determined using landmark-based analysis. A-F Mean landmark configurations of WT (Orange) and Dp1Tyb (Cyan) crania (**A-D**) and mandibles (**E, F**), showing lateral (**A**), superior (**B**), inferior (**C**) and rear (**D**) views of the cranium and lingual (**E**) and buccal (**F**) views of the mandible. **G-L** Displacement heatmaps after global size differences have been regressed out, produced by superimposing the mean shapes of the WT and Dp1Tyb crania (**G-J**) and mandibles (**K,L**), showing lateral (**G**), superior (**H**), inferior (**I**) and rear (**J**) views of the cranium and lingual (**K**) and buccal (**L**) views of the mandible. Red and Blue represent the distribution of expansion and contraction respectively in Procrustes (shape) distance. Regions of the Dp1Tyb mesh outside the WT mesh are coloured red, whereas any parts inside the WT mesh are coloured blue, thereby showing displacement relative to WT.

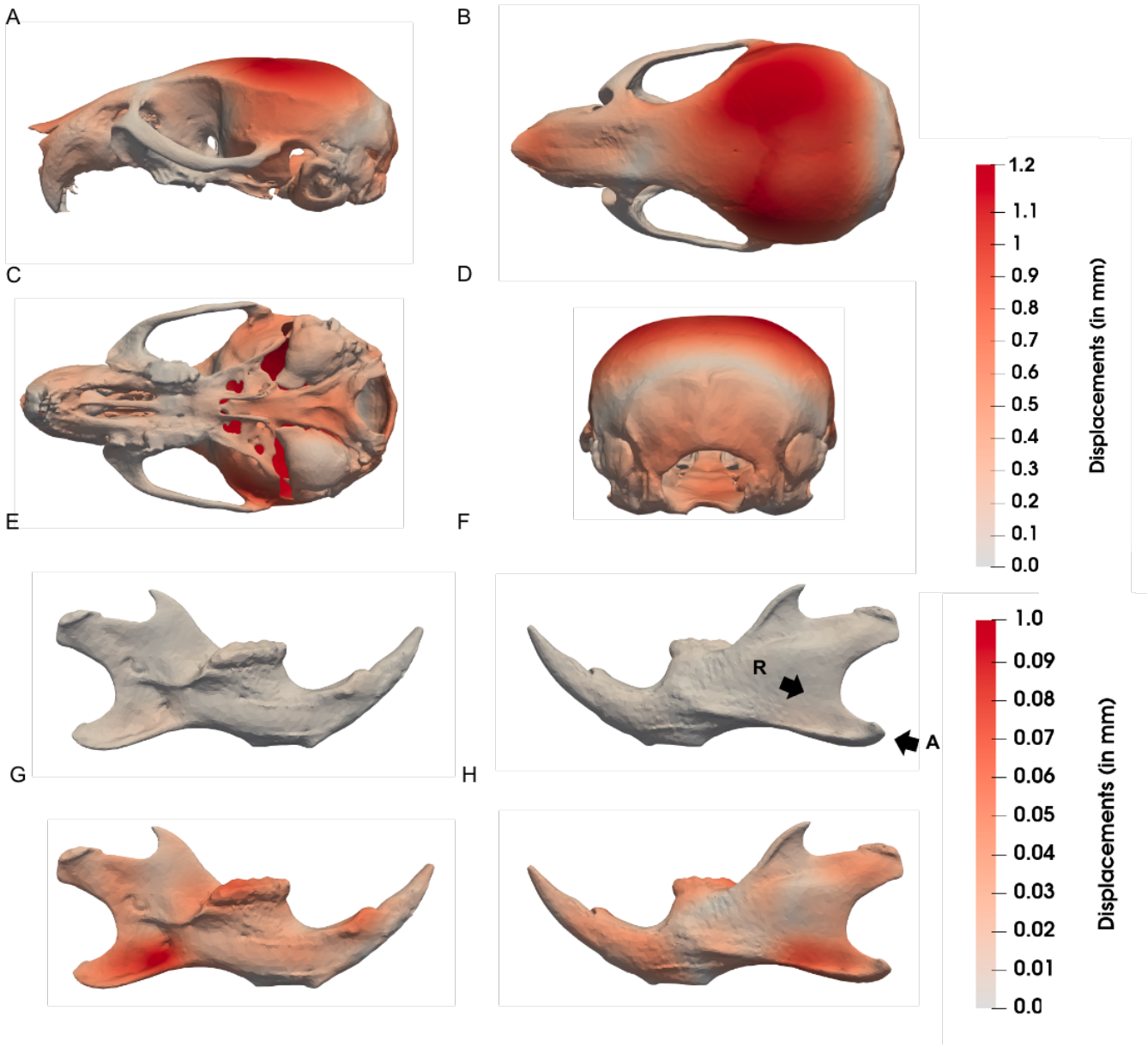

Figure 4. Visualisation of altered shape of Dp1Tyb crania and mandibles determined using landmark-free analysis. Displacement heatmaps after global size differences have been regressed out estimated using output momenta from the current-based atlas construction, showing locations of shape differences between WT and Dp1Tyb crania (**A - D**) and mandibles (**E-H**) , showing lateral (**A**), superior (**B**), inferior (**C**) and rear (**D**) views of the cranium and lingual (**E, G**) and buccal (**F, H**) views of the mandible. **A-F** are on the same colour scale; the colour scale in **G, H** maximises contrast for the mandibles only. Arrows **R** and **A** indicate the ramus and Angular process respectively.

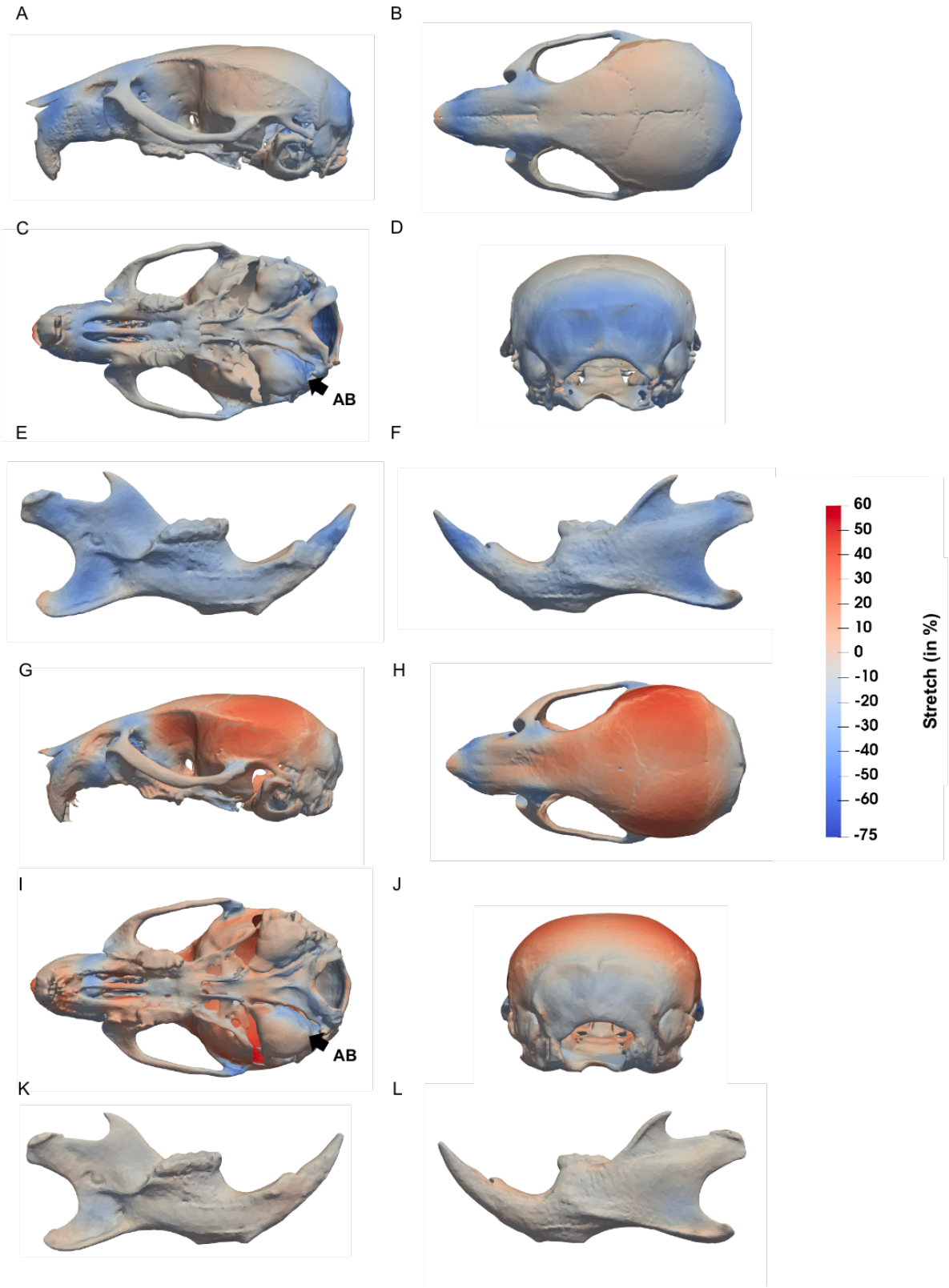

700 **Figure 5. Altered surface stretch in Dp1Tyb crania and mandibles determined using**
701 **landmark-free analysis.** Heatmaps show unscaled (**A-F**) or scaled (**G-L**) surface stretch
702 between WT and DS crania (**A-D, G-J**) and mandibles (**E-F, K-L**), showing lateral (**A,G**),
703 superior (**B,H**), inferior (**C,I**) and rear (**D,J**) views of the cranium and lingual (**E,K**) and buccal
704 (**F,L**) views of the mandible. Stretch changes were estimated using output momenta from
705 the current-based atlas construction. Note that global size changes were regressed out.
706 Arrow **AB** indicates the auditory bulla.

Supplementary Information

A landmark-free morphometrics pipeline: Application to characterise a Down syndrome model skull phenotype

Nicolas Toussaint[1]*, Yushi Redhead[2,3]*, Wei Liu[4], Elizabeth M. C. Fisher[5], Benedikt Hallgrimsson[4], Victor L.J. Tybulewicz[3,6§], Julia A. Schnabel[1§], Jeremy B.A. Green[2§]

[1] School of Biomedical Engineering and Imaging Sciences, King's College London, London, UK
[2] Centre for Craniofacial Biology & Regeneration, King's College London, London, UK
[3] The Francis Crick Institute, London NW1 1AT, UK
[4] Department of Cell Biology & Anatomy, University of Calgary, Calgary AB T2N 4N1, Canada
[5] UCL Institute of Neurology, London, WC1N 3BG, UK
[6] Department of Immunology & Inflammation, Imperial College London, London W12 0NN, UK

*Equal contribution

[§]Correspondence to:
JAS (email: julia.schnabel@kcl.ac.uk), VLJT (email: Victor.T@crick.ac.uk), or to
JBAG (email: jeremy.green@kcl.ac.uk)

Supplementary Videos

Supplementary Video 1.

Cranium morph including size

Cranium morph between the mean WT and Dp1Tyb shapes, where size has not been regressed out. Derived from landmark-free analysis. Red and Blue colour change indicate expansion and contraction respectively as a percentage. Derived from landmark-free analysis.

Supplementary Video 2.

Mandible morph including size

Mandible morph between the mean WT and Dp1Tyb shapes, where size has not been regressed out. Red and Blue colour change indicate expansion and contraction respectively as a percentage. Derived from landmark-free analysis.

Supplementary Video 3.

Cranial morph displacement heatmap

Cranial morph between the mean WT and Dp1Tyb shapes, where size has been regressed out. Red colour change indicates the magnitude of displacement in mm. Derived from landmark-free analysis.

Supplementary Video 4.

Mandible morph displacement heatmap

Mandible morph between the mean WT and Dp1Tyb shapes, where size has been regressed out. Red colour change indicates the magnitude of displacement in mm. Derived from landmark-free analysis.

Supplementary Video 5.

Exaggerated Mandible Morph

Mandible morph between the mean WT and Dp1Tyb shapes, where size has been regressed out and the magnitude of the deformation has been exaggerated by a factor of 3. Derived from landmark-free analysis.

Supplementary Video 6.

Cranial Interior morph including size stretch heatmap

Cranial morph, showing the interior of the skull, between the mean WT and Dp1Tyb shapes, where size has not been regressed out. Red and Blue colour change indicate expansion and contraction respectively as a percentage. Derived from landmark-free analysis.

Supplementary Video 7.

Cranial Interior morph stretch heatmap

Cranial morph, showing the interior of the skull, between the mean WT and Dp1Tyb shapes, where size has been regressed out. Red and Blue colour change indicate expansion and contraction respectively as a percentage. Derived from landmark-free analysis.

Supplementary Video 8.

Mandible morph stretch heatmap

Mandible morph between the mean WT and Dp1Tyb shapes, where size has been regressed out. Red and Blue colour change indicate expansion and contraction respectively as a percentage. Derived from landmark-free analysis.

Supplementary Video 9.

Cranial morph stretch heatmap

Cranial morph between the mean WT and Dp1Tyb shapes, where size has been regressed out. Red and Blue colour change indicate expansion and contraction respectively as a percentage. Derived from landmark-free analysis.

Supplementary Video 10.

Cranial mesh points stretch heatmap

Landmark-free-derived heatmap of cranium local stretch with no scaling. The mesh is represented here as all the points of the mesh rather than a rendered surface. Red and Blue colour change indicate expansion and contraction respectively. Downloading and viewing in a paused video by moving the slider is recommended.

Supplementary Figures

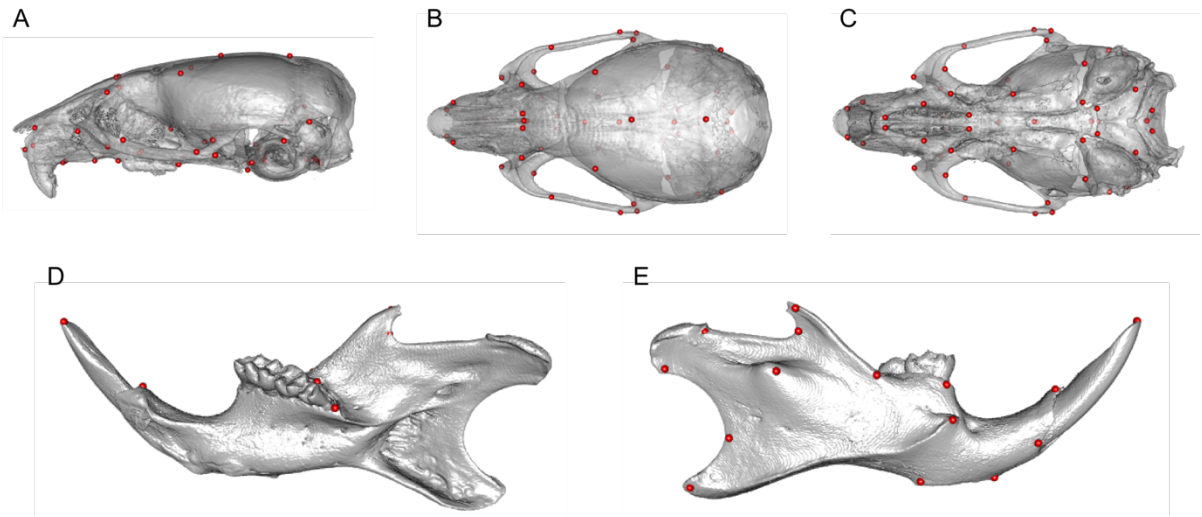

Supplementary Figure 1.

Location of landmarks used in landmark-based morphometric analysis. A-E Anatomic locations of landmarks shown on a 3D digitized image of a µCT scan as previously defined [1,2]. 68 cranial landmarks are shown on lateral (A), superior (B), and inferior (C) views of the cranium. 17 mandibular landmarks are shown on lingual (D) or buccal (E) views of the mandible.

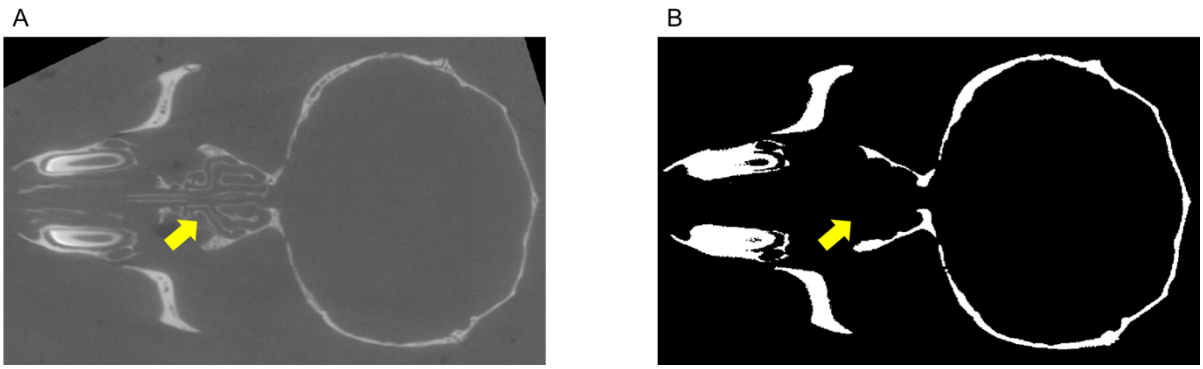

Supplementary Figure 2.

Planar view of mouse head captured by µCT. A Image pre-processing. **B** Image post-processing. Yellow arrow indicates cartilaginous element (nasal turbinate).

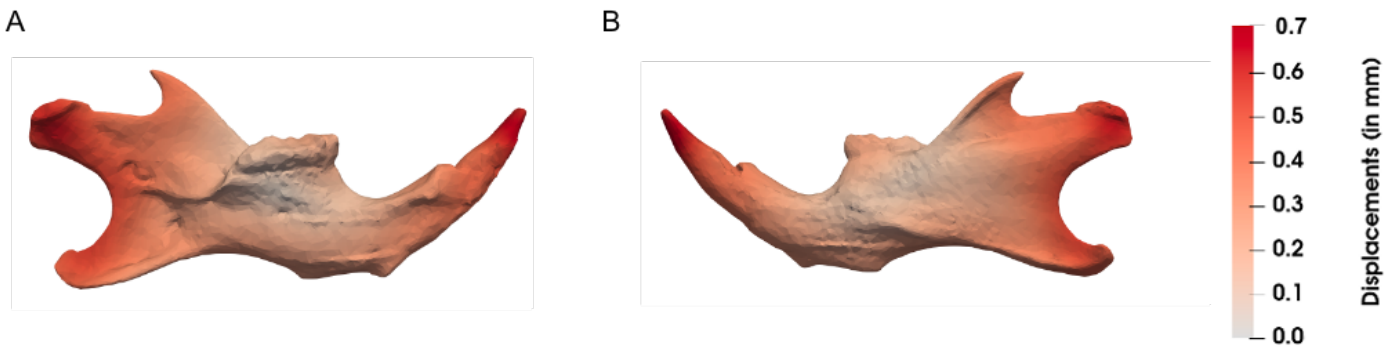

Supplementary Figure 3.

Displacement heat map with no scaling.

Without scaling, displacement changes are localised to the extremities.

\

Supplementary Table

		Mean Centroid Size in mm (± SEM)		difference	
		WT	**Dp1Tyb**	**absolute (mm)**	**percentage**
Landmark-based	**Cranium**	6.387±0.061	5.939±0.061	0.448	7.01%
	Mandible	4.502±0.038	4.204±0.038	0.298	6.62%
Landmark-free	**Cranium**	6.987±0.063	6.514±0.063	0.473	6.77%
	Mandible	4.025±0.041	3.768±0.041	0.257	6.39%

Supplementary Table.

Comparison of centroid sizes of crania and mandibles from WT and Dp1Tyb mice determined using landmark-based or landmark-free methods.

Supplementary References

1. Hallgrímsson, B., Lieberman, D. E., Liu, W., Ford-Hutchinson, A. F. & Jirik, F. R. Epigenetic interactions and the structure of phenotypic variation in the cranium. *Evol. Dev.* **9**, 76–91 (2007).
2. Hallgrímsson, B., Dorval, C. J., Zelditch, M. L. & German, R. Z. Craniofacial variability and morphological integration in mice susceptible to cleft lip and palate. *J. Anat.* **205**, 501–517 (2004).

Supplementary Appendix 1:

Landmark-free Morphometrics Pipeline Description

This Appendix is intended as an overview of the landmark-free pipeline for a relative non-specialist. Detailed dcoumentation is embedded with the pipeline code published on GitLab at https://gitlab.com/ntoussaint/landmark-free-morphometry. This Appendix is organised into five sections as follows:

A. Pipeline Dependencies
B. µCT Pre-processing
C. Mesh Alignment
D. Atlas Construction
E. Shape Statistics

A. Pipeline dependencies and notes on initialisation

All packages and software listed below are required. The pipeline is written in Python and C++ and requires a suitable environment to run both. We used the browser-based Juypiter environment (https://jupyter.org/). Specific requirements for each segment of the pipeline are listed at the appropriate page within the pipeline code but the complete list is as follows:

Absolutely required:

FSL - https://fsl.fmrib.ox.ac.uk/fsl/fslwiki (Image analysis tools)
Deformetrica - http://www.deformetrica.org/ (Atlasing tools)
Git - https://git-scm.com/ (Code version-control system)
ITK - https://itk.org/ (Segmentation and registration tools)
VTK - https://vtk.org/ (Visualisation tools)
CMake - https://cmake.org/ (Compiler)
Python packages:
- Matplotlib
- Numpy
- SimpleITK
- Vtk
- Pandas
- Seaborn

Software we used but for which there may be similar alternatives:

Meshlab - http://www.meshlab.net/ (Mesh decimation)
Itksnap - http://www.itksnap.org/pmwiki/pmwiki.php (Image manipulation tool)
Paraview - https://www.paraview.org/ (Image visualisation tools)
Mitk - http://mitk.org/wiki/The_Medical_Imaging_Interaction_Toolkit_(MITK) (Landmarking tool for coarse alignment)

The pipeline code is downloaded as landmark-free-morphometry-master.zip or ~.tar. After decompressing the package and moving to its directory within the Terminal app (Apple, Linux or equivalent in Windows) Juypiter is started using the command **ipython notebook** which opens the pipeline in the default system Web browser. The pipeline is presented as a series of virtual "pages" which contain "**cells**" (sections) of two types. One type defines a function, the other applies those functions to the data. Cells can be run individually or as an automatic sequence (see Juypiter documentation for details). An example of a function-defining cell is below:

Mesh extraction

mesh extraction from a binary image using Marching cubes and VTK

Short description of what the particular cell does and the inputs, outputs and adjustable parameters.

Black text is code and teal text is a comment on what the code does.

```
def extract_mesh(parcellation_file, output_mesh_file, smooth_NIter=20, smooth_relaxation=0.6):
    ''' Extract a mesh from a binary image using vtk

    The method uses Marching Cubes in order to extract a mesh outlining a binary segmentation image
    The mesh is then smoothed in order to avoid the pixelization effect

    @arg parcellation_file: input binary image file
    @arg output_mesh_file: output vtk mesh file
    @arg smooth_NIter: number of iterations for the smoothing filter
    @arg smooth_relaxation: Relaxation factor for the smoothing filter

    @ret: output_mesh_file
    '''

    import vtk

    ## read the input binary image
    reader = vtk.vtkMetaImageReader()
    reader.SetFileName(parcellation_file)
    reader.Update()
    ## perform marching cubes
    mc = vtk.vtkImageMarchingCubes()
    mc.SetInputConnection (reader.GetOutputPort())
    mc.ComputeNormalsOff()
    mc.ComputeGradientsOff()
    mc.ComputeScalarsOn()
    mc.SetValue(0, 0)
    ## smooth the output mesh
    smoother = vtk.vtkSmoothPolyDataFilter()
    smoother.SetInputConnection(mc.GetOutputPort())
    smoother.SetNumberOfIterations(smooth_NIter)
    smoother.SetRelaxationFactor(smooth_relaxation)
    smoother.FeatureEdgeSmoothingOff()
    smoother.BoundarySmoothingOn()
    ## write the output to file
    writer = vtk.vtkPolyDataWriter()
    writer.SetFileName(output_mesh_file)
    writer.SetInputConnection(smoother.GetOutputPort())
    writer.Write()

    return output_mesh_file
```

B. <u>µCT Pre-processing</u>

This section describes the code used to extract and produce a mesh from an initial µCT image. The following cells can be run with default values to define the required functions:

Binary Segmentation

- Defines functions used in the object extraction

Parcellation

- Defines functions required for parcellation of binary image

Mesh Extraction

- Defines function used in generating a mesh from a binary image

Mirror mesh file

- Defines function used to mirror the mesh file

Display help functions

- Defines functions used to display images within the notebook

Generic Imports

- Imports Numpy

Using **ITK-Snap** save µCT images in the **NIFTI** (.nii.gz) format.

The following five **cells** need to be edited to change parameters and filenames before running (N.B. annotations describe the sections that can or need to be changed, along with a brief description of inputs, outputs and function/s of the cell).

Load data

Loads in the image file to be processed.

Defines current working directory. Set the folder in which outputs are stored. This should not need to be changed as the 'data' and 'preprocessing' folders are already within the file along with the scripts.

```
working_directory = os.path.join(os.getcwd(), 'data', 'preprocessing')
input_image = os.path.join(os.getcwd(), 'data', 'uCT-1.nii.gz')
arr = display_image(input_image)
_ = plt.hist(arr.flatten(), np.linspace(0,15000,1000), density=True)
```

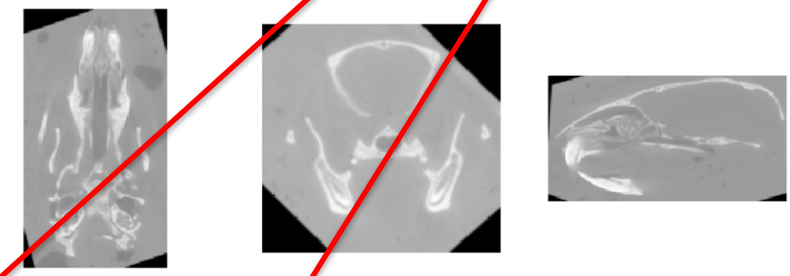

This tells the script where to look for the file to be processed. In this case within the **data** folder.

In this example uCT-1.nii.gz is the initial µCT image to be processed. This should be replaced with the filename desired.

Object extraction

The cell uses the functions defined in **object_extraction** to extract the object of interest from the input image and apply morphological functions to remove any noise and close unwanted holes.

Name of output file, a binarized image.

```
[9]: object_file = extract_major_object(input_image,
                                        os.path.join(working_directory,␣
↪'uCT-1_object.nii.gz'),
                                        threshold=9000,
                                        closing_kernel=1,
                                        opening_kernel=0)

arr = display_image(object_file)
```

Adjustable parameters **Threshold** – an appropriate value should be selected to extract the region of interest from the original µCT image. **Closing_kernel** and **opening_kernel** - parameters used to fill holes in the binary image. If none is required set to 0

Check output file using **ITK-Snap** to validate successful extraction of the region of interest. If the regions has been appropriately binarized it should be saved as **.mha** file.

Parcellation

This cell uses the functions defined in **parcellation** to 'parcellate' the image into various regions according to the density of the bone. This allows the separation of mandible (densest bone) from the rest of the skull. If no region separation is required skip this step and move to the **Mesh extraction** step:

Define the name for file to be segmented i.e. the file from **Object extraction**.

Watershed level should be .22 for full resolution image. (.1 is for the example data provided).

```
: region_file = parcellate_object(object_file,
                                  os.path.join(working_directory, 'uCT-1_regions.
↪mha'),
                                  watershedlevel=.1,
                                  shrink=1)

arr = display_image(region_file)
```

The output is a binary image with regions ordered by bone density. Use **ITK-Snap** to visualise these labels. The example on the right shows these regions, here label one is the red region. Note the label/s for region of interest (ROI).

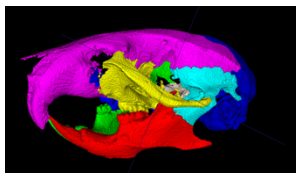

Object selection

Input the labels of relevance to separate the ROI from the rest of the subject.

Define the file name for the selected region of interest. This is the output file from **region parcellation**.

Input labels of regions to be extracted from the **region parcellation** step prior.

If only the first label is required, input 1 for both the lower threshold (l_threshold) and upper threshold (u_threshold). If the first 2 labels are desired set the values to 1 and 2 respectively. If the whole image is desired input the lowest and highest label numbers.

```
[11]: selectedobject_file = select_object(region_file,
                                          os.path.join(working_directory,␣
      ↪'uCT-1_selectedobject.mha'),
                                          l_threshold=1,
                                          u_threshold=1)

      arr = display_image(selectedobject_file)
```

Check the output in **ITK-snap** opening it as a **segmentation file.** Any noise or irrelevant regions can be removed using the paint brush tool.

Extract mesh

This step uses functions defined in **Mesh Extraction** to extract a surface mesh from the region of interest selected prior. The meshes generated are in the **.vtk** format.

Output mesh file name.

```
[12]: mesh_file = extract_mesh(selectedobject_file,
                               os.path.join(working_directory, 'uCT-1_regions.vtk'),
                               smooth_relaxation=.2)
      png_file = display_mesh(mesh_file,
                               os.path.join(working_directory, 'uCT-1_regions.png'))
```

Mesh files produced are large in size and increase computational time of the **Atlasing** step to unrealistic durations. To overcome this, meshes were decimated using **meshlab**.

Save meshes in the **.stl** (stereolithography) format using paraview. Open the mesh in meshlab and apply **quadric edge collapse decimation** fi and enter the percentage reduction desired (authors used 0.15).

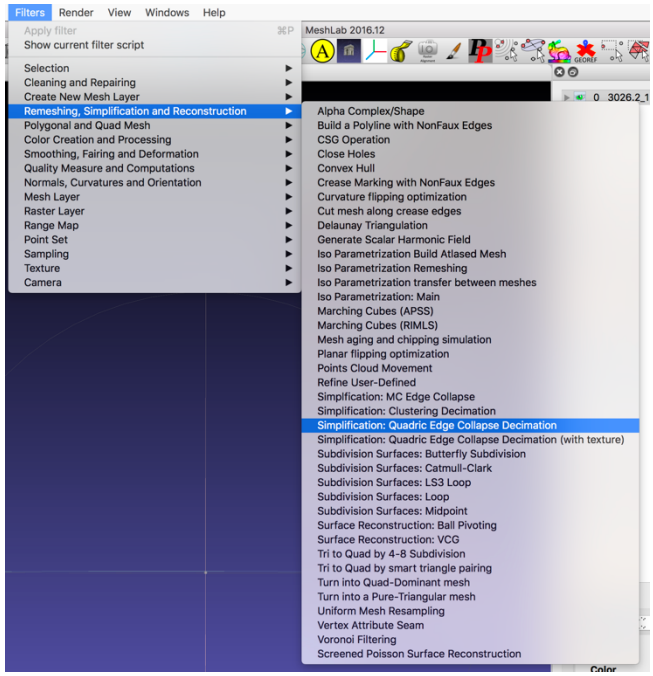

Once meshes for all subjects are generated move to the next step, **Mesh Alignment.**

C. Mesh Alignment

This section describes the process of aligning the meshes produced in the previous section. Initial coarse alignment is required to allow the Atlasing process (below) to work. This first requires manually placing a small number of landmark using **Mitk-Workbench**, minimally three (e.g. for a hemi-mandible) or more usually three symmetrically placed pairs. Landmark file names should be identical to the mesh file name e.g. Mandible_1.vtk, with its landmark file, Mandible_1.mps.

Below is shows landmarks used to align the mandible.

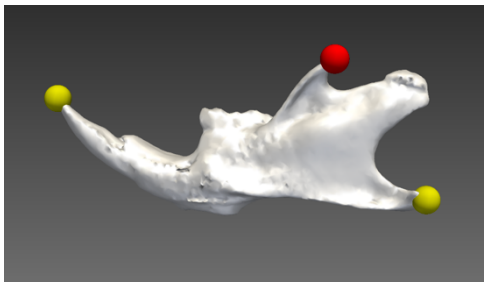

Once complete move landmark files (.mps) and mesh files (.vtk) into Alignment folder.
The following are run with default values:

Read landmarks

- Defines functions used to import landmark files

Numpy – vtk help functions

- Define functions used convert landmark files so they can be used to align meshes
- Functions used to extract centroid and centroid size

Procrustes alignment

- Defines functions used in alignment
  - Rigid – rigid body alignment
  - Similarity – rigid body plus scaling alignment

Load data

Loads meshes and associated landmark files ready for alignment,

Mesh Alignment

Uses functions defined in **Procrustes alignment** to align meshes. Two modes can be selected, **Similarity** or **Rigid body**. "Similarity" aligns meshes whilst regressing out the size. "Rigid body" aligns meshes but maintains size differences:

Here, define the folder in which the pipeline will search for inputs and store outputs. By default, it is set to the alignment folder within data.

```
[8]: %matplotlib inline

### General Imports
from glob import glob
import os

working_directory = os.path.join(os.getcwd(), 'data', 'alignment')

### Find meshes and landmark files
meshfiles      = glob('{}{}*.vtk'.format(working_directory, os.sep))
landmarksfiles = glob('{}{}*.mps'.format(working_directory, os.sep))


meshfiles[:] = [el for el in meshfiles if not (('initial_template.vtk' in el)␣
 ↪or ('_r.vtk' in el)) ]

### assert similar size and sort lists
assert(len(meshfiles) == len(landmarksfiles))
meshfiles.sort()
landmarksfiles.sort()

%matplotlib inline
import os
from matplotlib import pyplot as plt
pngfilename = os.path.join(os.getcwd(), 'Images', 'unaligned-meshes.png')
plt.figure(figsize=(10,10))
plt.imshow(plt.imread(pngfilename))
plt.axis('off')
plt.show()
```

Choose mode here to ‘**Similarity**’ or ‘**Rigid body**’

```
[9]: output_meshes = align_meshes_to_center(meshfiles, landmarksfiles,␣
     ↪mode='similarity', output_directory=working_directory, suffix='_r')

moving 1.vtk towards center with landmarks 1.mps -- determinant: 1.07
moving 2.vtk towards center with landmarks 2.mps -- determinant: 0.94
```

Adds a suffix to aligned mesh files so they can easily be distinguished from the original unaligned files.

Mesh alignment fidelity should be checked in **Paraview**.

D. Atlas Construction

This section describes the application of the shape averaging and comparison (atlasing) processes.
Within the **atlasing** folder (included in the pipeline package) there are three files adjustable files:

Model.xml describes parameters for deformation:
– kernel-width: Order of magnitude of displacements for the template
– kernel-width: Order of magnitude for the subjects’ displacements

model.xml

```
<?xml version="1.0"?>
<model>
    <model-type>BayesianAtlas</model-type>
    <template>
        <object id="mandible">
            <deformable-object-type>NonOrientedSurfaceMesh</deformable-object-type>
            <data-sigma>10</data-sigma>
            <kernel-type>p3m</kernel-type>
            <kernel-width>2.0</kernel-width>
            <filename>initial_template.vtk</filename>
        </object>
    </template>
    <deformation-parameters>
        <kernel-width>1.5</kernel-width>
        <kernel-type>p3m</kernel-type>
        <number-of-timepoints>10</number-of-timepoints>
    </deformation-parameters>
</model>
```

Optimization_parameters.xml describes parameters that drive the minimization procedure:
– max-iterations: Stop criterion for iterations, usually ~150
– number-of-threads: Number of threads to use, usually equal to the number of subjects (should not exceed the number of threads available on the system)

optimization_parameters.xml

```
<?xml version="1.0"?>
<optimization-parameters>
    <initial-step-size>0.01</initial-step-size>
    <max-iterations>150</max-iterations>
    <number-of-threads>16</number-of-threads>
    <save-every-n-iters>5</save-every-n-iters>
    <smoothing-kernel-width-ratio>0.5</smoothing-kernel-width-ratio>
</optimization-parameters>
```

Data_set.xml defines the files to be atlased and should be structured as follows:

data_set.xml

```
<?xml version="1.0"?>
<data-set>
    <subject id="1_r.vtk">
        <visit id="experiment">
            <filename object_id="mandible">1_r.vtk</filename>
        </visit>
    </subject>
    <subject id="2_r.vtk">
        <visit id="experiment">
            <filename object_id="mandible">2_r.vtk</filename>
        </visit>
    </subject>
</data-set>
```

From the alignment folder transfer aligned meshes (files with suffix **_r**) and initialtemplate.vtk into the atlas folder.

Deformetrica

The first cell loads the **Deformetrica** software. If the software is not found an error is returned.

```
[ ]: def which(program):
         ''' Search for a program on disk
         '''
         import os
         def is_exe(fpath):
             return os.path.isfile(fpath) and os.access(fpath, os.X_OK)

         fpath, fname = os.path.split(program)
         if fpath:
             if is_exe(program):
                 return program
         else:
             for path in os.environ["PATH"].split(os.pathsep):
                 exe_file = os.path.join(path, program)
                 if is_exe(exe_file):
                     return exe_file

         return None

     deformetrica_location = which('deformetrica')
     if deformetrica_location is None:
         print('deformetrica error: Please install the deformetrica library: www.
      ↪deformetrica.org')
     else:
         print('Found deformetrica at this location: {}'.
      ↪format(deformetrica_location))
```

Launch Simulation

Launches the atlasing software using the files and parameters defined by model.xml, optimisation_parameters.xml and data_set.xml.
Deformetrica.log, within the output folder, contains information on the progress of the atlas, including the number of control points and the current iteration.

```
[ ]: import os

     working_directory = os.path.join(os.getcwd(), 'data', 'atlasing')
     script_filename = os.path.join(working_directory, 'deformetrica.sh')
     os.system('bash {}'.format(script_filename))
```

E. Shape statistics

This section describes the statistical analysis of the outputs from the atlas.
Atlasing generates several output files of which the following three are used for statistical analysis:

- **Atlas_controlpoints.txt**
    - Control points of the atlas
- **Atlas_momenta.txt**
    - Momentum vectors of the atlas
- **Atlas_initial_template.txt**
    - Average mesh of the population

These files are must be moved into the **shape statistics** folder. In the same folder, a user-populated file **data.csv** defines the names and types of the subjects.

data.csv example file
In this example in GroupId, 1 refers to a mutant and -1 to WT, and in Gender, 1 Male and -1 female.

	A	B	C
1	id	GroupId	Gender
2	33.4a	-1	-1
3	33.4b	-1	-1
4	35.1c	-1	-1
5	37.1c	1	1
6	38.1c	-1	1
7	29.3d	-1	1
8	29.3g	-1	1
9	30.3b	-1	-1
10	30.3d	1	-1

The following cells are the run with default values:

Imports
- Loads relevant packages required for this section of the pipeline

Deformetrica
- Loads deformetrica ready to be used (required for creation of morphs)

Load data
- Loads output files stated previously to be analysed

Define population's groups
- Loads data.csv

Subgroup definitions
- Assigns names to groups of specimens defined by one or more parameters in **data.csv**.

[Default groups are: WTf (Wildtype female, defined by: group ID = -1, gender = -1, CRf is defined by: group id = 1, gender =-1), WTm (Wildtype Male), CRf (Carrier female) and CRm (Carrier Male)]
However, the user should change the names and definitions of subgroups to suit their needs.

```
In [48]: g1 = df['GroupId'].values < 0
         g2 = df['GroupId'].values > 0

         WTf = list(df.loc[(df['GroupId'] < 0) &
                           (df['Gender']  < 0)].index)
         WTm = list(df.loc[(df['GroupId'] < 0) &
                           (df['Gender']  > 0)].index)
         CRf = list(df.loc[(df['GroupId'] > 0) &
                           (df['Gender']  < 0)].index)
         CRm = list(df.loc[(df['GroupId'] > 0) &
                           (df['Gender']  > 0)].index)
```

Kernel Principal Component Anaylsis (kPCA)
This cell runs a principal component analysis (PCA) and produces a classification score (as a percent) and a p value for said score. As well as defining group IDs (by default group one > 0

and group two < 0 using values set in **data.csv**) and calculating the mean Principal Component score.

Cross validation score and standard deviation

Cross validation score and p value of permutation test

```
SVM Classification score 0.90 +/- 0.07)

/Users/yushi/anaconda3/lib/python3.6/site-packages/sklearn/model_selection/_split.py:598: FutureWarning: You should s
pecify a value for 'n_splits' instead of relying on the default value. The default value will change from 3 to 5 in v
ersion 0.22.
  warnings.warn(NSPLIT_WARNING, FutureWarning)

Classification score 0.90 (pvalue : 0.0010)

<Figure size 504x360 with 0 Axes>
```

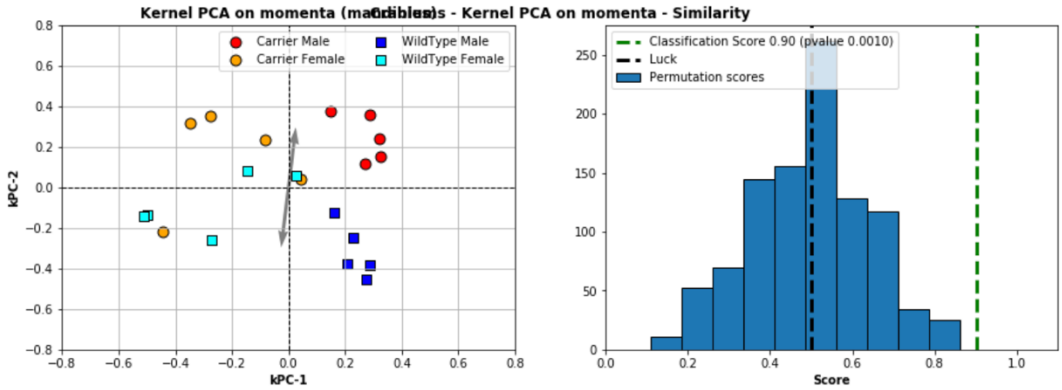

Eigenvalues/Eigenvectors

Produces Eigenvalues and eigen vectors. Providing data on how much variability each principle component describes.

Write PCA points on disk

Produces an excel file, kpca.csv containing the PC values which can exported to produce PCA graphs.

Momenta projection

Produces momenta that describes project between the mean of the whole population to the means of the previously defined populations.

Shoot mean shape between groups

Uses the momenta projection to 'shoot' the shape towards the means of the two groups.

Shooting outputs

Saves the shot meshes produced in the previous step in two locations:

- data/shapestatistics/shooting/forward
- data/shapestatistics/shooting/backward

They correspond to the mean shape (**Atlas_initial_template.vtk**) displaced towards the mean of group one (backward) and the mean of group two (forward). Each file now contains several meshes. The first mesh in the folder is the average shape of the whole population and the last mesh the mean shape of the subgroup. Each mesh in-between represents a step of deformation moving from one to the other.

Cyclic deformations between subgroups

Reorders the mesh files produced in **Shooting outputs** to generate a cyclic shape change starting with the mean of group one to the mean of group two and back again. The files for the cyclic deformation are saved in: data/shapestatistics/shooting/combined. Files should be opened in **Paraview** to visualise the meshes.

The deformation is viewed cyclically, by pressing the repeat and play buttons.

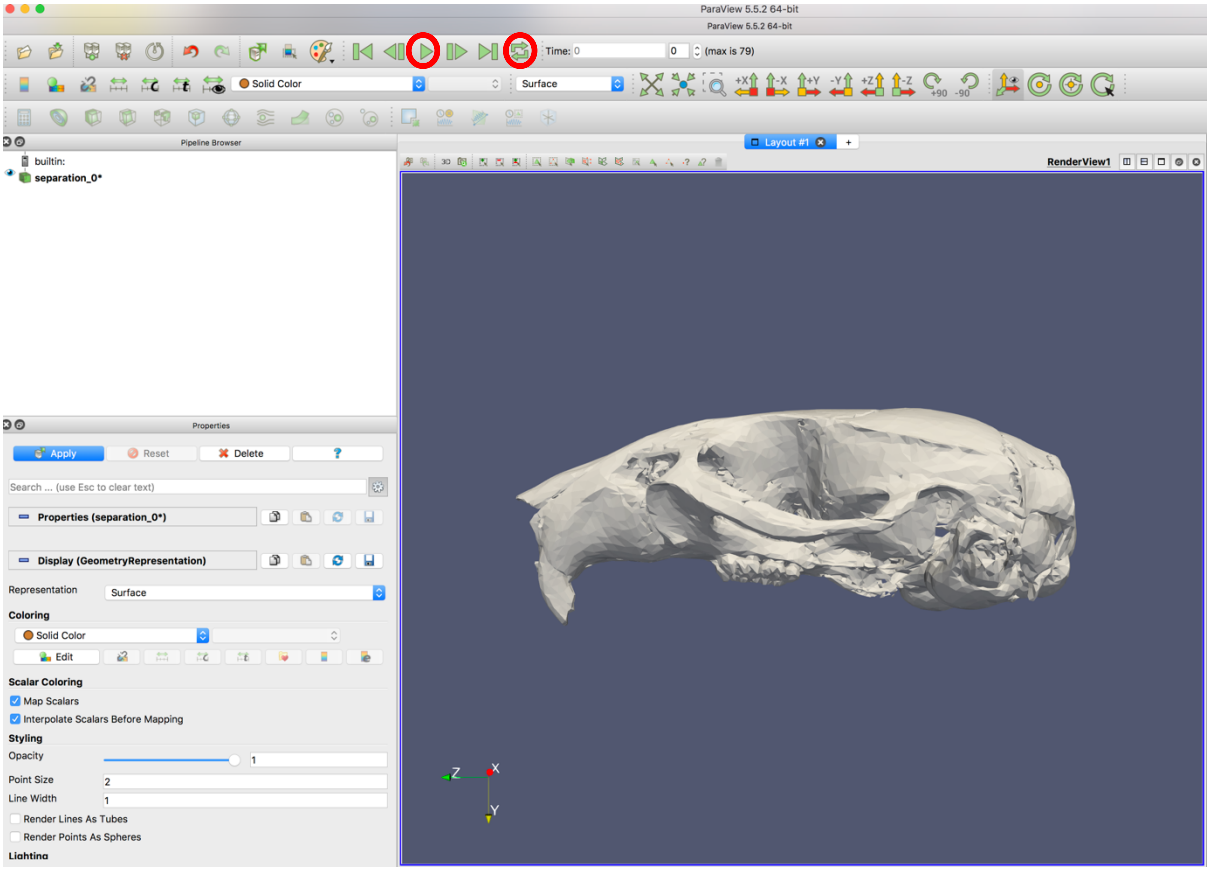

"Stretch" map (Local volume change map) between groups

This step integrates data on displacement and stretch into the cyclic deformation produced in the previous step. Removing the # from in front of **compute_point_displacements** calculates displacement.

```
    compute_point_displacements(m, mean, m)
    #compute_cell_surfaces_differences(m, mean, m)
    #compute_absolute_cell_surfaces_differences(m, mean, m)
    ### write mesh
    writer = vtkPolyDataWriter()
    writer.SetInputData(m)
    writer.SetFileName(mfile)
    writer.Update()

cyclic_combination(meshfiles1, meshfiles2, os.path.join(shooting_directory, 'combined'))
```

Removing the # from in front of **compute_cell_surfaces_difference**, calculates stretch.

```
    #compute_point_displacements(m, mean, m)
    compute_cell_surfaces_differences(m, mean, m)
    #compute_absolute_cell_surfaces_differences(m, mean, m)
    ### write mesh
    writer = vtkPolyDataWriter()
    writer.SetInputData(m)
    writer.SetFileName(mfile)
    writer.Update()

cyclic_combination(meshfiles1, meshfiles2, os.path.join(shooting_directory, 'combined'))
```
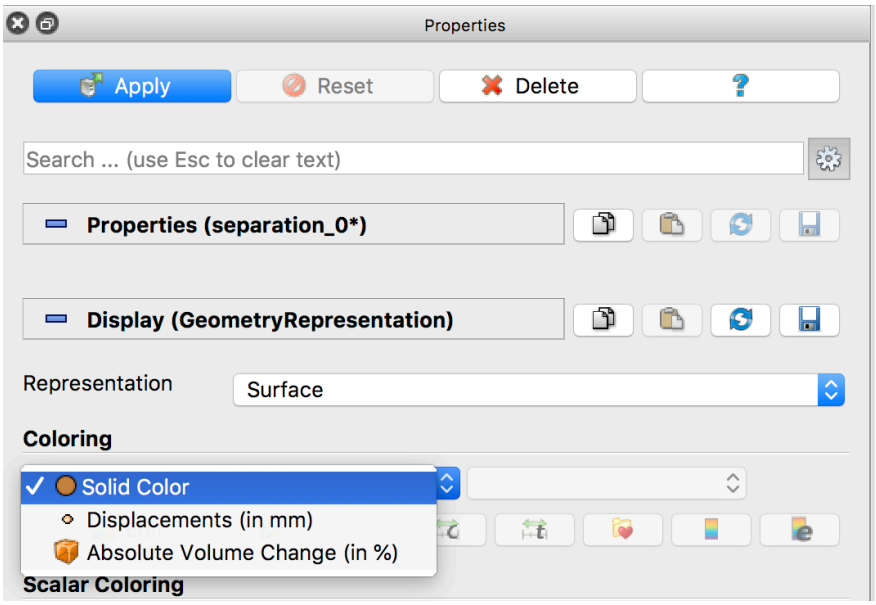
Heat maps are viewed by importing the mesh files from the combined folder into **Paraview**. Select displacements or Absolute Volume from the colouring drop down menu and the morph was played as before to visualise the heat maps. Colour scale (look-up table) may need to be adjusted to visualise differences properly.